Applied Catalysis B: Environmental 284 (2021) 119813

Contents lists available at ScienceDirect

Applied Catalysis B: Environmental

journal homepage: www.elsevier.com/locate/apcatb

Deactivation and activation mechanism of TiO_2 and rGO/Er^{3+}-TiO_2 during flowing gaseous VOCs photodegradation

Zepeng Rao [a,b], Guanhong Lu [a], Asad Mahmood [a], Gansheng Shi [a], Xiaofeng Xie [a,*], Jing Sun [a,*]

[a] State Key Lab of High Performance Ceramics and Superfine Microstructure, Shanghai Institute of Ceramics, Chinese Academy of Sciences, 1295 Dingxi Road, Shanghai 200050, China
[b] University of Chinese Academy of Sciences, 19 (A) Yuquan Road, Beijing 100049, China

ARTICLE INFO

Keywords:
rGO/Er^{3+}-TiO_2
Photocatalyst
Gaseous VOC
Degradation pathway
Deactivation
Activation

ABSTRACT

The poor efficiency and stability of photocatalysts are the fundamental issues to be addressed for photodegrading VOCs in practical applications. Herein, 0.5 wt%rGO/0.5 mol%Er^{3+}-TiO_2 (0.5rGO/0.5 ET) exhibited the excellent performance and a remarkable durability towards gaseous VOC (*o*-xylene), while pure TiO_2 (PT) and 0.5 mol% Er^{3+}-TiO_2 (0.5 ET) showed poor catalytic activity and deactivation after 60 min. The results suggested that intermediates accumulation was primarily responsible for the deactivation of PT and 0.5 ET. In contrast, the activity of 0.5rGO/0.5 ET was not decreased although more intermediates were generated compared with other samples. The experiments revealed that rGO provide more adsorption sites for the intermediates, which helped 0.5rGO/0.5 ET resist the deactivation even after photodegradation of 10 h and 4 cycles. Therefore, rGO played a vital role in keeping the stable activity of the composites. This study is helpful to understand the deactivation/activation mechanism of photocatalysts and provided a promising strategy to make catalyst in activation for industrial application.

1. Introduction

Low boiling point organic pollutants, e.g., volatile organic compounds (VOCs; aldehydes, ketones, and aromatics) are the product of several natural processes and industrial operations, for example, *o*-xylene and its derivatives are released from industrial production, volatilization of plastic and paint products, dismantling of electronic wastes, production of organic solvents and chemical coatings, etc [1,2]. This leads to constantly increasing of VOCs in both indoors as well as outdoors environment. Studies have shown that indoor air is 2–5 times more polluted than outdoor air [3]. The exposure to VOCs could cause serious health issues, i.e., nausea, respiratory problems, dizziness, liver damage, and cancer [4,5]. Additionally, VOCs are accountable for the formation of urban smog and depletion of the ozone layer in the troposphere [6]. Therefore, it is fundamental to develop techniques for safe removal of VOCs from the atmosphere.

Recently, photocatalytic oxidation (PCO) technology has been widely considered for the pollution control, which has the advantage of operating under ambient conditions. PCO technology has shown some promising results both in the solution phase as well as gas-solid reactions [7,8]. Also, the oxide-based semiconductor materials, such as TiO_2, used in the photodegradation reactions are inexpensive, stable and nontoxic [9]. Studies directed on the photodegradation of several VOCs have shown that these organic pollutants could be oxidized to CO_2 and water under light irradiation [9,10]. In this regard, much attempt has been reported to study reaction kinetics, optimize the reactor design, comprehend the deactivation mechanism of catalysts and the effect of light sources in the course of VOCs removal [11–14]. Among them, one crucial problem encountered in the real application of PCO is the deactivation of photocatalysts in the degradation process. The deactivation of the material might be due to the implicit behavior of a photocatalyst, low stability, or adsorption of intermediates during a photodegradation reaction covering the active surface sites, which will eventually impede the surface catalyzed reaction. Among them, intermediates accumulation will result in changing the properties of photocatalyst surface, including the decrease of adsorption sites, the reduction of reactive sites, the obstruction of photogenerated carrier migration and the diminish of free radical production, etc. To overcome these issues, several strategies have been adopted, which include impurities doping in the TiO_2 crystal lattice, self-doping, morphology control, surface modification through co-catalysts, and compositing with other semiconductor materials [15–18]. For example, some reports

* Corresponding authors.
E-mail addresses: xxfshcn@163.com (X. Xie), jingsun@mail.sic.ac.cn (J. Sun).

https://doi.org/10.1016/j.apcatb.2020.119813
Received 22 September 2020; Received in revised form 1 December 2020; Accepted 5 December 2020
Available online 10 December 2020

mentioned that carbonaceous deposits (coke) led to the inactivation of photocatalysts during the photodegradation of VOCs [19,20]. Lu et al. suggested carbon deposition (coking) on the active sites, sintering of gold nanoparticles and the rearrangement of active TiO_2 were responsible for $Au/TiO_2/SiO_2$ catalysts deactivation in propylene epoxidation reaction [17]. However, indirect strategies, more specifically, reducing the generation of main intermediates were used to inhibit deactivation of photocatalysts, which does not provide an inherent solution to overcome the performance lost during the photodegradation of VOCs.

Recently, rare earth (RE) ions doping has shown some promising results during the removal of VOCs, which substantially improve the photogenerated e^{-}-h^{+} pair's separation and light-harvesting of TiO_2, leading to the high photocatalytic activity of the Er^{3+}-doped TiO_2. This behavior might be due to the incorporation of new energy states (RE-4f states) and the up-conversion process (UCP) [21–24]. Our previous research reported that RE ions doping increases the photocatalytic activity, but unfortunately, the accumulation of intermediates during the VOCs photodegradation process have been observed to lower the overall performance of Er^{3+} doped TiO_2 systems [23]. To overcome this issue, the combination with carbon materials, such as the reduced graphene oxide (rGO), can significantly boost the overall photocatalytic performance of TiO_2. This is because rGO has a large specific surface area, the high mobility and superior thermal conductivity [25,26], which improve not only the absorptivity but also the charge separation efficiency. However, researchers have not recognized that the large π-bond structure of rGO could provide adsorption sites not only for the initial aromatic VOCs but also for the aromatic intermediates generated during degradation. Thus, the photocatalyst has less chance to be contaminated due to the low occupation of the reactive sites on the catalyst surface. In this way, rGO might play a significant role in preventing the deactivation of the photocatalyst.

Therefore, it is anticipated that a combination of rGO with Er^{3+}/TiO_2 nanoparticles (rGO/Er^{3+}-TiO_2) will further enhance the photocatalytic properties. Additionally, the accumulation of intermediates, the yield of free radicals, and changes in the superficial structure and properties (including the stability of host structure) of catalysts are the key factors affecting the photocatalytic activity. It is meaningful to study the dominant factors in detail which affect the deactivation of photocatalysts. To understand how rGO influence the transfer and separation of interfacial charges, the generation of free radicals and the accumulation of intermediates for a rational photocatalyst design.

Herein, rGO/Er^{3+}-TiO_2 photocatalysts were synthesized to study the photodegradation of aromatic ring containing o-xylene. For comparison, pure TiO_2 and Er^{3+}-TiO_2 were also studied. To understand the role of rGO played on the structural, optical and photochemical properties, a series of characterization tests were carried out. Several sets of experiments revealed that the introduction of rGO provided adsorption sites for intermediates from the degradation of o-xylene, which led to long-term photocatalytic activity of the catalyst. The possible oxidation pathway on the as-synthesized photocatalyst, the deactivation and activation mechanism of photocatalytic performance were proposed in this work.

2. Experimental

2.1. Materials

Titanium (IV) isopropoxide (TIP) (97 %) and $Er(NO_3)_3{\cdot}6H_2O$ (99.9 %) were obtained from Sigma–Aldrich. Acetic acid and ethanol (Zhenxing Co., Ltd) were used as solvents. Nitric acid, potassium ferricyanide and potassium ferrocyanide trihydrate were produced by the Aladdin Industrial Co. 5,5-dimethyl-1-pyrroline N-oxide (DMPO) was purchased from Sigma Chemical Co. All chemicals were used as received without further purification.

2.2. Preparation of TiO_2, Er^{3+}-TiO_2 and rGO/Er^{3+}-TiO_2 photocatalysts

Pure and Er^{3+}-TiO_2 samples were synthesized via a sol-gel method. The specific procedure as published in our previous work [23]. GO was prepared by a modified Hummer's method [27]. rGO/Er^{3+}-TiO_2 nanocomposites were synthesized via a facile impregnation method. In a typical process, a predetermined amount of the 0.5 mol%Er-TiO_2 powders and GO were added to a beaker (50 mL) containing deionized (DI) water (20 mL) and ethanol (10 mL) solution under magnetic stirring. Then an appropriate amount of nitric acid was dropped into the above suspension solution to adjust the pH to 2 under vigorous stirring for 16 h. Subsequently, the obtained suspension was washed 3 times with DI water and ethanol after being centrifuged. Finally, the products were put into a muffle furnace and calcined at 350 °C for 3.5 h. The pure and Er modified TiO_2 samples are marked as pure TiO_2 (PT) and 0.5 % $molEr^{3+}$-TiO_2 (0.5 ET). The nanocomposite material is designated as 0.5 wt%rGO/0.5 %$molEr^{3+}$-TiO_2 (0.5rGO/0.5 ET), where 0.5 wt% is the mass ratio of rGO to TiO_2. In addition, coupling pure TiO_2 with rGO was used as a reference sample labeled as 0.5rGO/PT. The combination of GO and Er^{3+}-TiO_2 sample without any heat treatment is used as a comparison sample and noted as 0.5 wt%GO/0.5 %$molEr^{3+}$-TiO_2 (0.5GO/0.5 ET).

2.3. Characterization

The surface morphology was studied using a scanning electron microscope (SEM; SU9000). The in-depth microstructure analysis was performed using high resolution transmission electron microscope (HRTEM; JEM-2100) operating at 200 kV. X-ray diffraction (XRD) profiles were collected by a D8 ADVACE diffractometer (Bruker). The Brunauer − Emmett − Teller (BET) specific surface area (S_{BET}) data were obtained by ASAP 3000 instrument. Raman spectra were performed on a DXR spectrometer. UV–vis Diffuse reflectance spectroscopy (DRS) spectra were analyzed by a Lambda 950 apparatus (Perkin–Elmer). The PHI-5000C ESCA instrument was used to measure X-ray photoelectron spectroscopy (XPS) spectra. LS55 spectrometer was used to collect photoluminescence (PL) spectra. The photocurrent and electrochemical impedance spectroscopy (EIS) results were performed on an electrochemical workstation (CHI660D). electron spin resonance (ESR) signals were carried out on a JES-FA200 measurement. *o*-Xylene-temperature programmed desorption (TPD) and NH_3-TPD plots were conducted on a ChemiSorb PCA-1200 instrument. *in situ* diffuse reflectance infrared Fourier transform spectroscopy (DRIFTS, IRTracer-100), gas chromatography-mass spectrometer (GC–MS, TSQ 8000 Evo), temperature-programmed oxidation (TPO), thermogravimetric-mass spectrometry (TG-MS STA449 F3 + QMS403D) and intermediates desorption (ID)-TPD was employed to analyze the absorbed intermediates on the surface of photocatalysts. The detailed process was presented in supporting information.

2.4. Adsorption and photocatalytic properties

The adsorption and photodegradation properties of VOC were assessed in an automated measurement setup, which is composed of a sample holder, gas-flow monitory system, and a coupled GC (Scheme S1). In our test system, the feed gases were supported by the three-in-one generator and carried with water by humidifier before reaching the mixer. We can control the relative humidity (RH) of water by adjusting the flow rate of carrier gas and the amount of water in the humidifier. The RH was set to 65 % to simulate the similar condition in air, which can basically reflect our real living environment to some extent. The adsorption behavior of *o*-xylene on photocatalysts was studied through dynamic adsorption-desorption analysis under the dark condition. The flow rate and the initial concentration of *o*-xylene are 20 standard cubic centimeter per minute (sccm) and 25 ppm, respectively. The incident integrated irradiance of the lamp on the sample is 51.2 mW/cm^2. The

adsorption amount (X) of VOC was calculated by equation:

$$X = C_0 \times \rho_1 \times \rho_2 \times \left\{ \left[\int_0^t v \times \left(1 - C/C_0\right) dt \right]_{catalyst} - \left[\int_0^t v \times \left(1 - C/C_0\right) dt \right]_{blank} \right\} / \left(M \times m\right)$$

where C_0 (ppm) represent initial concentration of *o*-xylene and C are the real-time concentration of the target gas at each time interval. ρ_1 (g cm^{-3}) and ρ_2 depict air density and relative vapor density of the gas-phase VOC, t (min) is the time for each data recording, v (mL min^{-1}) is the VOC flux rate, M (g mol^{-1}) and m (g) stand for molar mass of the selected VOC and the mass of the sample used, respectively. The photocatalytic activity was determined by the removal ratio of gas-phase *o*-xylene. The photocatalytic efficiency (PE) of VOC was noted as PE = (C_0 – C)/C_0 × 100 %. The mineralization rate (MR - selectivity of CO_2) of *o*-xylene was calculated by formula [28]: MR(%) = [(CO_{2out})-(CO_{2in})] /[8 × ρ × (C_{in}) × PE(%)] × 10000, where CO_{2out} and CO_{2in} are the outlet and inlet concentrations of CO_2. C_{in} and PE(%) represent the inlet concentration and photocatalytic efficiency of gas-phase *o*-xylene, respectively.

3. Results and discussion

3.1. Morphology, structural and photoelectrochemical characteristics of photocatalysts

Fig. 1 shows the morphology of the as-prepared samples, where the average particle size of Er-doped TiO_2 catalyst decreased (Fig. 1a ~ b), which suggested that Er doping can restrain the grain growth of the sample to some extent. Further evidence was provided by Scherrer equation (Table 1), where the crystallite size of samples decreased from 13.9 to 10.0 nm after incorporating Er ions, while the particle size and grain size of 0.5 ET sample did not change significantly after being combined with rGO (Fig. 1c and Table 1, 10.0 nm of 0.5 ET and 10.3 nm of 0.5rGO/0.5 ET). 0.5 ET nanoparticles distributed on both sides of the rGO sheets and the agglomeration of nanoparticles was improved, which is conducive to the charge transfer between 0.5 ET and rGO. In addition, the thickness of the added rGO was in the range of 3 ~ 5 nm, and the lattice fringe spacing was 0.35 nm associated with the (101) facet of anatase (Fig. 1d). The inset selective area electron diffraction (SAED) pattern confirmed the well crystalline nature of the sample.

Table 1
Unit cell parameters, the specific surface area (S_{BET}) of PT, 0.5 ET and 0.5rGO/0.5 ET samples.

Sample	V (Å^3)	Crystallite size (nm)	S_{BET} (m^2/g)
PT	136.21	13.9	25.14
0.5 ET	136.64	10.0	51.57
0.5rGO/0.5 ET	136.67	10.3	53.33

X: adsorption capacity, X^a: adsorption capacity on per specific surface area.

The as-synthesized photocatalysts showed pure anatase phase in XRD profiles (Fig. S1a). This was further confirmed by Raman spectra (Fig. S2a). Besides, no diffraction peak of graphene was observed in the XRD patterns, which might be due to low rGO content [29]. As shown in Table 1, there is no obvious change in the unit cell volume of 0.5rGO/0.5 ET (136.64 Å^3) compared with 0.5 ET (136.67 Å^3). The specific surface area increased from 26.14 to 51.57 m^2/g after the introduction of Er ions, which could be associated with the decreasing particle size. Interestingly, the S_{BET} of 0.5rGO/0.5 ET (53.33 m^2/g) sample did not change significantly in contrast to 0.5 ET (51.57 m^2/g). Hence, the above results suggested that the addition of rGO has almost no influence on the morphology, structural properties, and specific surface area of 0.5 ET sample. However, the absorption edge of catalyst exhibited a clear redshift after coupling with rGO sheets (Fig. S1b), indicating that coupling rGO with Er^{3+}-TiO_2 helped improve the light-harvesting of the composite. In contrast to pure TiO_2, Er^{3+} doping induced additional up-conversion absorption peaks, which might be due to the f-f electronic transitions of Er^{3+} ions [30,31]. This behavior could facilitate the utilization of light, thereby enhancing the photocatalytic performance of the catalyst.

The D (1353 cm^{-1}) and G (1598 cm^{-1}) peaks of graphene were

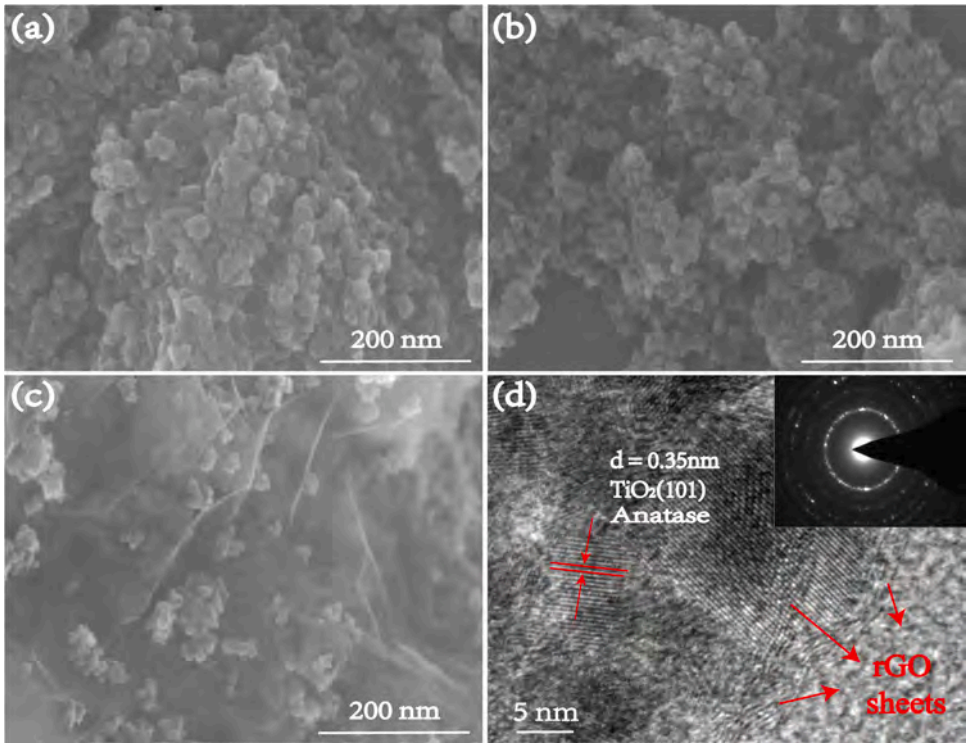

Fig. 1. SEM images of (a) PT, (b) 0.5 ET, and (c) 0.5rGO/0.5 ET catalyst, and (d) HRTEM image of 0.5rGO/0.5 ET sample before photocatalytic reaction.

observed in the enlarged Raman spectra (Fig. S2b), where the I_D/I_G value increased from 0.32 (in 0.5GO/0.5 ET) to 0.64 after heat treatment (Table S1), indicating that GO was effectively reduced to rGO [32,33]. Additionally, the atomic proportion of O to C decreased from 1.91 (in 0.5GO/0.5 ET) to 1.14 (Fig. S2d and e, and Table S1), further confirming the effective restoration of GO [29]. This improved the conductivity of GO, facilitating the electron transfer between 0.5 ET and rGO. Meanwhile, the Raman characteristic peaks at 618 and 635 cm^{-1} moved to low wavenumbers located at 616 and 633 cm^{-1} (Fig. S2c) and the Ti 2p broad bands at 457.72 and 463.52 eV relatively shifted to 457.64 eV and 463.42 eV after 0.5 ET combination with rGO (Fig. S2f), which confirmed the formation of a chemical interface (Ti-O-C) in 0.5rGO/0.5 ET sample [34]. This will improve the electron dynamics at the interface between TiO_2 and rGO, and ultimately enhancing the catalytic activity.

3.2. Photocatalytic activity of catalysts and degradation path of gaseous *o*-xylene

Fig. 2 shows that the photocatalytic performance of the modified TiO_2 towards gaseous *o*-xylene substantially improved in contrast to pure TiO_2. 0.5rGO/0.5 ET sample completely removed the target pollutants (Fig. 2a), which suggested that combination of rGO is an effective way to improve the photocatalytic activity of TiO_2. We have recently disclosed that the enhanced photocatalytic efficiency of 0.5 ET sample was associated with the special electronic structure (Er-4f states), which promoted charge separation, and thereby produced more free radicals [23,35]. The increased photocatalytic activity of 0.5rGO/0.5 ET can be attributed to the combination of rGO, which will eventually improve the electron-transfer at the interface between TiO_2 and rGO [25,34]. Furthermore, after the addition of RE ions and rGO, the formed RE-4f states in nanocomposite lowers the transition barrier among electrons between TiO_2 and rGO, which further increased the separation efficiency of e^--h^+ pairs, and finally facilitated the production of free radicals [29]. This behavior was confirmed by PL, photocurrent density, and ESR results of DMPO- $^{\bullet}O_2^-$ and DMPO- $^{\bullet}OH$ adducts. As displayed in Fig. S3a, the PL intensity of the nanocomposite decreased, which could be associated with the improved charge transfer and hole-electron separation efficiency in 0.5rGO/0.5 ET composite [36]. The enhanced photocurrent intensities and the decreased radius of EIS Nyquist plots further confirmed that the separation process of photoinduced carriers was promoted (Fig. S3b and c) [37,38], thereby leading to the increase of free radical production (Fig. S3d and e), and ultimately improving the photocatalytic activity. The order of maximum removal efficiency was as follows (Fig. 2c): 0.5rGO/0.5 ET (100 %) > 0.5 ET (74.2 %) > PT (39.1 %). And the maximum mineralization rate of 0.5rGO/0.5 ET, 0.5 ET and PT was 58.2 %, 50.5 % and 30.8 %, respectively (Fig. 2b and c), which was lower than the removal rate of *o*-xylene. This indicated that *o*-xylene cannot be completely mineralized into CO_2 and water, and the difference is ascribed to the formation of intermediate species. The deactivation of PT and 0.5 ET led to the decrease of CO_2 concentration after 60 min of irradiation during the *o*-xylene degradation (Fig. 2a). Thus, GC–MS was used to analyze the generated intermediates (Fig. S4 and Table S2). As presented in Fig. S5, the types and relative abundance of intermediates on 0.5 ET was lower than that of PT. This might be due to the fact that 0.5 ET had more free radicals to further oxidize byproducts of the parent compound degradation than PT (showing Fig. S3d and e). Notably, PT and 0.5 ET catalyst showed deactivation after 60 min of irradiation, but 0.5rGO/0.5 ET still maintained an excellent photocatalytic performance after 240 min. This indicated that the introduction of rGO played a crucial role in keeping the photocatalytic activity of 0.5rGO/0.5 ET.

The *in situ* DRIFTS analysis was further used to comprehend the adsorption and degradation process in detail. As shown in Fig. 3a, the bands located at 3568, 1446 cm^{-1}, which were due to the ν(OH) vibrations of aromatic ring (2-methylbenzyl alcohol) under light illumination [39,40]. Peaks at 3070, and 2955, 2870 cm^{-1} were attributed to the ν(C–H) stretching vibrations of aromatic ring and $-CH_3$ (*o*-xylene

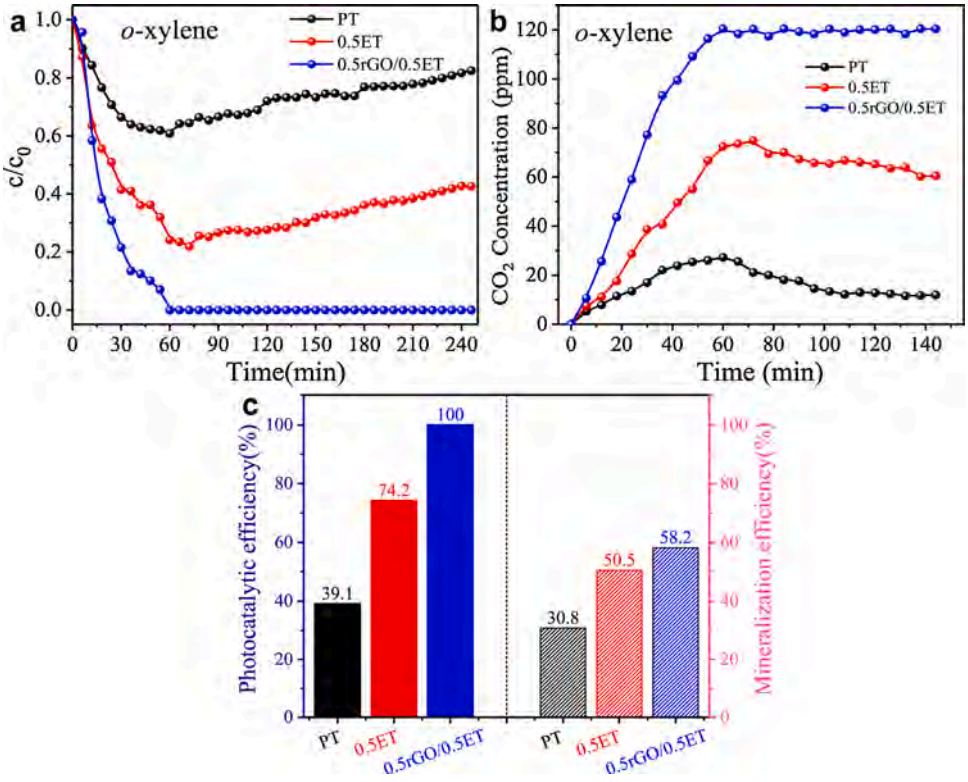

Fig. 2. (a) The degradation and (b) CO_2 generation curves for *o*-xylene with 0.1 g sample illuminated by a 400 W xenon lamp, and (c) histogram of photocatalytic efficiency and mineralization rate.

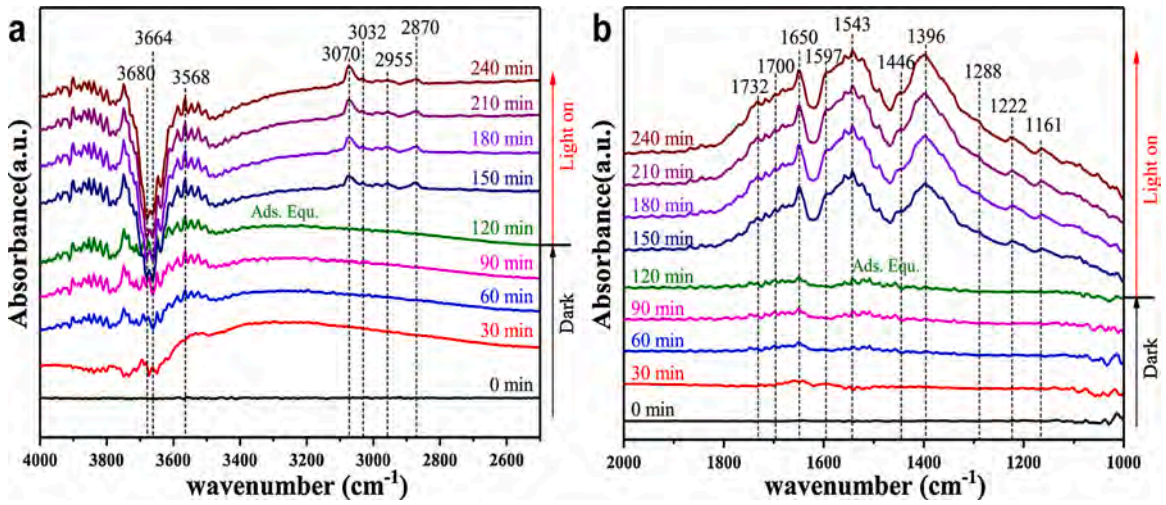

Fig. 3. *in situ* DRIFTS spectra of dark adsorption and photocatalytic degradation processes of o-xylene over 0.5rGO/0.5 ET surface under UV light irradiation (250 W) in the range of (a) 4000 – 2500 cm^{-1} and (b) 2000 – 1000 cm^{-1}.

and toluene), respectively [41,42]. The peak at 3032 cm^{-1} was associated with the *ν*(C–H) stretching vibrations of the benzene ring (benzene) [43,44]. As presented in Fig. 3b, a peak at 1732 cm^{-1} can be attributed to the C═O stretching vibration of aliphatic species (acetone, butanol, 5-methyl-4-octanone) [45,46]. Weak bands at 1700 and 1222 cm^{-1} were identified as the *ν*(C═O) vibration of aromatic aldehyde (*o*-tolualdehyde) [39,47], 1650, 1597, 1543 cm^{-1} could be ascribed to the skeleton vibration *ν*(C═C) of the benzene ring [45,48]. The peak at 1288 cm^{-1} was identified as the *ν*(C—O—C) vibration of the anhydride species (phthalide) [49]. The peak at 1161 cm^{-1} was attributed to the C—OH vibration *ν*(C—OH) of aliphatic alkoxides species (butanol). The negative peaks at 3680 and 3664 cm^{-1} could be assigned to the stretching vibration of surface OH species *ν*(OH) on 0.5rGO/0.5 ET sample, suggesting that water was generated during the photocatalytic reaction. The GC—MS was further used to confirm the intermediate species (Fig. S4, S5 and Table S2). Combining with the *in situ* DRIFTS and GC—MS results, we proposed the possible photodegradation routes of *o*-xylene. As shown in Fig. S6, *o*-xylene (No. 1) was firstly oxidized into unopen-ring compounds, including 2-methylbenzyl alcohol (No. 10), *o*-tolualdehyde (No. 9), phthalide (No. 11), toluene (No. 3) and benzene (No. 4) [35–37], which were further photodegraded into chain products, such as 5-Methyl-4-octanone (No. 5), butanol (No. 6), butanone (No. 7) and acetone (No. 8), and finally mineralized into water and CO_2 (No. 2).

3.3. Deactivation mechanism of the photocatalyst

The deactivation of a photocatalyst limit its industrial applications, thus it is of utmost significance to study the durability of photocatalysts. As indicated in Fig. S7, PT and 0.5 ET samples possessed a stable crystal structure showing the pure anatase phase after 120 min of photodegradation. Additionally, UV–vis and electron microscopy studies provided the confirmation that the microstructure and optical properties of the catalyst did not change significantly after photocatalytic reaction (Fig. S8 and S9). These results can be inferred as that the inactivation was associated with the change of surface states and not due to its internal crystal structure. Thus, the lowering of the photocatalytic activity could be due to the change of the catalyst surface state.

Fig. 4 shows that the surface of the photocatalyst gradually turned yellow with increasing reaction time (0–120 minutes). Interestingly, the yellow color on the surface gradually disappeared when stopping the *o*-xylene flow and keeping light on. When the light illumination time reached 2 h (120–240 minutes), the sample returned its original color which suggested that most of the yellow matters (intermediates) were decomposed under light irradiation. GC–MS results confirmed this speculation (Fig. S10), where 7 kinds of intermediates were detected on the PT surface after 120 min of photodegradation while only acetone and CO_2 products appeared when we cut off the *o*-xylene supply while keeping the light irradiation on (up to 2 h). After being illuminated for 2 h, the treated sample was used to decomposed *o*-xylene again, the photocatalytic performance of the catalyst was restored or regenerated (360 – 420 min). Furthefore, after 120 min of photocatalytic reaction, the deactivated PT and 0.5 ET samples was taken out and placed in the atmospheric environment where sunlight can be injected through glass windows. PT and 0.5 ET gradually retained their own original color and

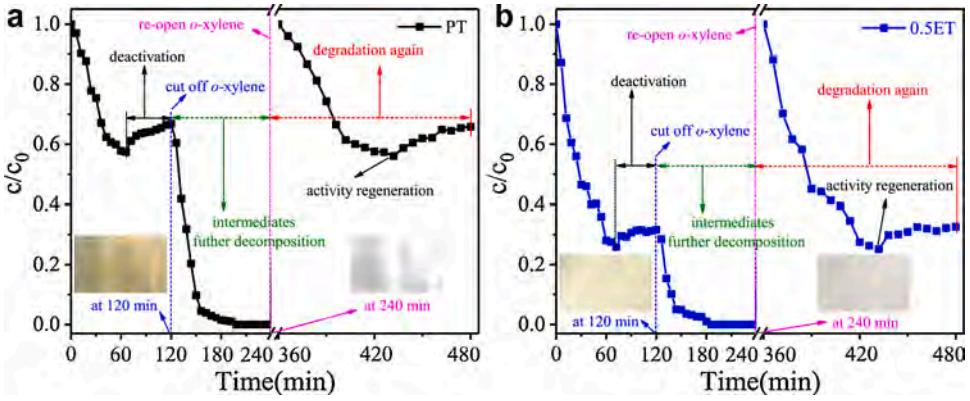

Fig. 4. The photodegradation plots of (a) PT and (b) 0.5 ET samples under the condition of cutting off and reopening *o*-xylene inlet, the inset images show changes on catalyst surface at 120 and 240 min. Initially, cutting off *o*-xylene and keeping light on when photocatalytic reaction reached 120 min. Next, after further decomposition of the byproducts under xenon lighting for 2 h (from 120 to 240 min), the sample was used to test the photocatalytic performance again (from 240 to 480 min, where the range of 240 – 360 min represents dark adsorption process).

the photocatalytic activities of the two samples were regenerated after 7 and 5 days exposing themselves to the atmosphere, respectively (Fig. S11). These observations suggested that the yellow matters on the photocatalyst surface was a key factor leading to the deactivation of samples. Previous studies have shown that the accumulation of the generated intermediates on the catalyst surface caused the catalyst to turn yellow [50]. GC–MS results in Fig. S5a further confirmed this mechanism, in which the yellowing surface of PT sample changes to its original color after most of the byproducts was eliminated. Therefore, these results suggested that intermediates accumulation induced the deactivation of materials. Additionally, the yellow color of PT surface (Fig. 4a) was more obvious than that of 0.5 ET (Fig. 4b). This indicated that more intermediate species generated on PT compared with 0.5 ET (confirmed by GC–MS results in Fig. S5), causing 0.5 ET to be slowly deactivated than PT. This result was due to the generation of more free radicals in 0.5 ET in contrast to the PT samples (Fig. S3d and e), suggesting that photocatalytic materials, which can produce more free radicals, can delay the inactivation of photocatalysts in the process of VOC degradation. A similar behavior was observed in our previous work [23].

In order to further understand the essential reason of catalyst deactivation caused by the accumulation of intermediate products, a series of experiments, including photocurrent, PL, EIS and ESR test were carried out. The photocurrent, PL and EIS tests were used to investigate the migration, separation, recombination and capture of photogenerated e^--h^+ pairs in PT and 0.5 ET materials during the removal of gaseous *o*-xylene (Fig. 5 and Fig. S12 and S13). Photocurrent intensities of PT sample decreased as the degradation time increased from 0 to 60 and 120 min under a continuous flow of *o*-xylene (Fig. 5a), which suggested that the transfer of photoinduced electrons to the electrolyte is obstructed from the electrode surface. This might be due to the presence of intermediate species on the pure TiO_2 surface, which form a film-like morphology and cover the reactive sites, which could capture the electrons at the electrode/electrolyte interface. After turning off *o*-xylene flow, while keeping the light on, the photocurrent intensities of samples were gradually increased with increasing irradiation time from 1 (180 min) to 2 h (240 min). This confirmed that the intermediate species covered on the surface were responsible for the lower photocurrent density. The PL and EIS test also support this interpretation, which demonstrated a high charge recombination under illumination time from 0 to 120 minutes (Fig. 5b and Fig. S12). After cutting off the gases, the decreased PL intensities and the radius of the EIS Nyquist curves indicated that the separation ability of carriers gradually recovered with light on from 120 to 240 min. A similar phenomenon was observed in 0.5 ET sample (Fig. S13). Hence, these data further suggested that intermediates accumulation was a dominant factor leading to the deactivation of PT and 0.5 ET samples.

The production of hydroxyl radicals ($^{\bullet}OH$) and superoxide radicals ($^{\bullet}O_2^-$) was associated with the separation process of photogenerated electron-holes [51], thereby affecting the oxidation of intermediate products. The characteristic intensity ratio of 1:2:2:1 for $^{\bullet}OH$ adducts and 1:1:1:1 for $^{\bullet}O_2^-$ in PT sample decreased as the photodegradation time increased to 120 min [52], indicating that the yield of $^{\bullet}OH$ and $^{\bullet}O_2^-$ radicals decreased in the elimination of *o*-xylene (Fig. S14a and b). This might be due to the fact that intermediates covered some reactive sites on the catalyst surface which progressively depressed the production of free radicals. However, the intensities of $^{\bullet}OH$ and $^{\bullet}O_2^-$ species gradually increased with increasing the exposure time from 1 (180 min) to 2 h (240 min) after cutting off *o*-xylene flow at 120 min. This is because the intermediate products were gradually decomposed and the active sites exposed with increasing of the light time, resulting in the continuous generation of free radicals. The yield of free radicals was restored when the irradiation time reached 2 h (240 min). As shown in Fig. S14c and d, similar trends can be seen in the 0.5 ET sample. Based on the above discussion, it could be concluded that intermediates accumulation occupied most of reactive sites, resulting in depressing the formation of free radicals, and thereby inducing the decrease of the photocatalytic activity [18,19]. Therefore, the accumulation of intermediates was a dominant factor to result in the deactivation of PT and 0.5 ET photocatalysts.

3.4. Activation mechanism of 0.5rGO/0.5 ET photocatalyst

0.5rGO/0.5 ET catalyst exhibited efficient and endurable photocatalytic activity even after photocatalytic reaction of 10 h and four cycles (Fig. 6a and b), which was attributed to the hybridization with rGO. Thus, a series of experiments were carried out to understand the essential reasons for the non-deactivation of 0.5rGO/0.5 ET and the role of rGO played in degradation process of gas-phase *o*-xylene. ID-TPD and TPO experiments were firstly used for qualitative and semi-quantitative analysis of the intermediates adsorbed on the photocatalyst surface after *o*-xylene photodegradation. As shown in Fig. S15a, the desorbed intermediates peaks of the investigated samples located at 300 ℃ - 750 ℃, where the order of desorption bands number was recorded as: 0.5rGO/0.5 ET > PT > 0.5 ET. This indicated that the produced byproducts of 0.5rGO/0.5 ET were more than that of 0.5 ET catalyst. *o*-Xylene-TPD and TPO test further confirmed this mechanism. As observed in Fig. S16, the chemical desorption peak (814 ℃) and the band intensities of 0.5rGO/0.5 ET were obviously higher than that of 0.5 ET (763 ℃), showing that rGO promoted adsorption of contaminants on the sample. The TPO

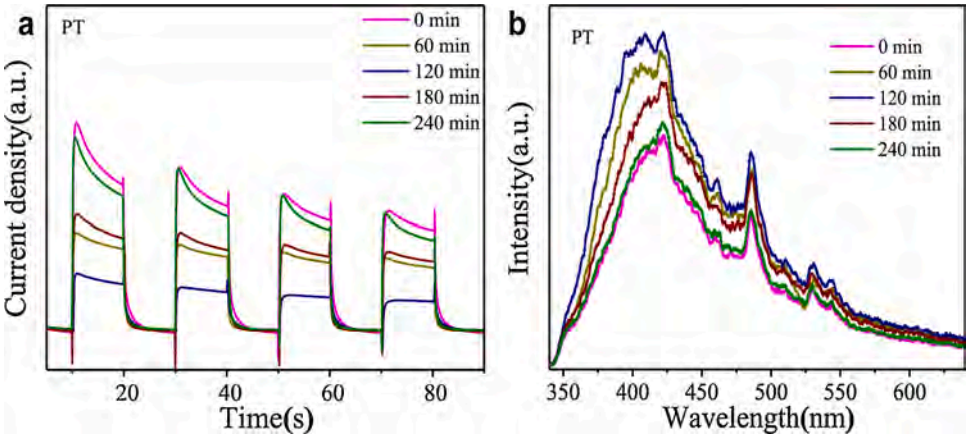

Fig. 5. (a) Photocurrent response and (b) PL plots of PT sample during the degradation process of *o*-xylene, in which 0, 60 and 120 min of photocurrent and PL curves are photocatalytic reaction for 0, 60 and 120 min, respectively. 180 and 240 min of plots represent the sample irradiated by xenon lamp for 1 and 2 h without introducing *o*-xylene.

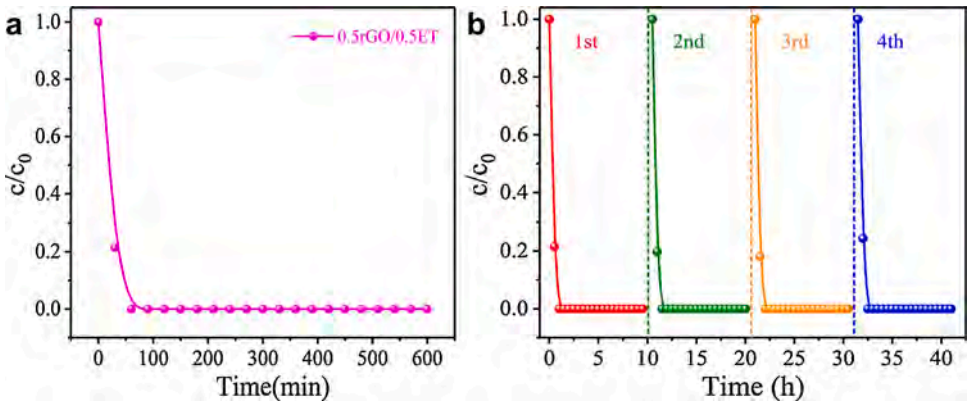

Fig. 6. Photocatalytic degradation plots of 0.5rGO/0.5 ET catalyst towards gaseous *o*-xylene under continuous irradiation for (a) 600 min and (b) four-cycle.

bands of 0.5rGO/0.5 ET, 0.5 ET and PT centered at 200 ℃- 588 ℃, 182 ℃- 470 ℃ and 212 ℃- 525 ℃, respectively, and the relative intensities of 0.5rGO/0.5 ET were higher than that of PT and 0.5 ET (Fig. S15b). These results suggested that both the types and levels of intermediate products in 0.5rGO/0.5 ET were larger than those of 0.5 ET and PT, which are in good agreement with the GC—MS data.

TG-MS analysis was used to identify the quantities and types of byproducts after photocatalytic reaction of gas-phase *o*-xylene (Fig. 7). As displayed in Fig. S17, before the photodegradation of *o*-xylene, the weight loss of PT, 0.5 ET and 0.5rGO/0.5 ET was respectively recorded as 1.26 %, 1.83 % and 2.60 % under argon flux. After photocatalytic reaction with *o*-xylene for 240 min, the weight loss of PT, 0.5 ET and 0.5rGO/0.5 ET were respectively increased to 3.09 %, 2.56 % and 5.03 % (Fig. 7a ~ c). Thus, the content of the accumulated intermediates for PT, 0.5 ET and 0.5rGO/0.5 ET was calculated as 1.83 %, 0.73 % and 2.43 %, this phenomenon further illustrated that the more intermediates were formed on the 0.5rGO/0.5 ET surface. Intermediate species gradually desorbed from the catalyst surface with increasing temperature, where main fragments (*m/z*) 30 (hydrocarbon), 43 (acetone or Butanone or 5-Methyl-4-octanone), 56 (butanol), 65 (*o*-tolualdehyde), 77

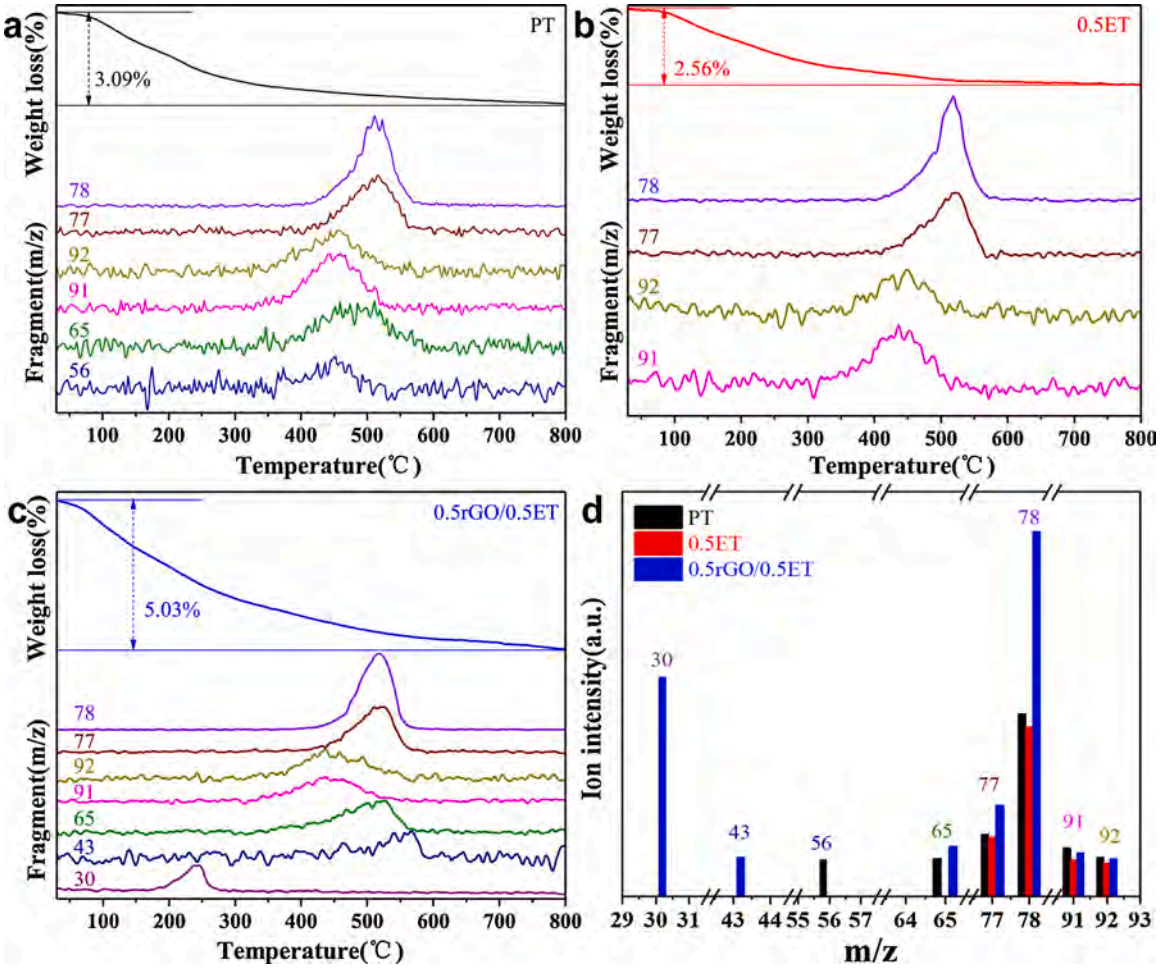

Fig. 7. TG-MS spectra of (a) PT, (b) 0.5 ET, (c) 0.5rGO/0.5 ET photocatalysts (50 mg) after photodegradation of *o*-xylene for 240 min, and the histogram of the detected main fragments (*m/z*).

(phenyl), 78 (benzene), 91 (*o*-xylene or 2-methylbenzyl alcohol) and 92 (toluene) desorbed at 245 ℃, 566 ℃, 451 ℃, 528 ℃, 518 ℃, 436 ℃ and 449 ℃. Additionally, Fig. 7a, d and Table S3 showed the detected fragments on the surface of PT were 56, 65, 77, 78, 91 and 92. The minimum numbers and quantities of intermediates (77, 78, 91, 92) were formed on 0.5 ET sample (Fig. 7b and d). As shown in Fig. 7c, d and Table S3, the maximum including 30, 43, 65, 77, 78, 7991 and 92 were generated in 0.5rGO/0.5 ET.

According to the above discussion, intermediates accumulation is a dominant factor leading to the deactivation of photocatalytic materials. As presented in Fig. S5 and Fig. 7, GC–MS and TG-MS show that 0.5rGO/0.5 ET possessed more kinds and highest concentration of byproducts in contrast to PT and 0.5 ET catalysts, where 10 kinds of main components were generated in nanocomposite while 7 and 5 types of main intermediates were produced on PT and 0.5 ET samples. However, 0.5rGO/0.5 ET sample still kept efficient catalytic performance towards *o*-xylene until photocatalytic degradation for 600 min (Fig. 6a). To investigate that more intermediate products were generated on the surface of 0.5rGO/0.5 ET catalyst without causing the catalyst to deactivate, several sets of tests including dynamic adsorption, photocurrent response, EIS, PL and ESR were carried out. As shown in Fig. S18, S8 and S9, after photocatalytic reaction of 240 min, 0.5rGO/0.5 ET presented stable anatase phase structure, microstructure and the optical properties, indicating that the non-deactivation of nanocomposite was not due to the change of its own structure. Hence, rGO played a vital role in the activation (non-deactivation) of photocatalytic performance.

Fig. 8a shows the dynamic adsorption characteristics of PT, 0.5 ET and rGO/0.5 ET towards gas-phase *o*-xylene. The adsorption ability of the photocatalyst was significantly enhanced after being modified with Er ions and rGO (Fig. 8b), in which the adsorption amount of 0.5 ET (1.79 μmol g^{-1}) was higher than that of PT (0.84 μmol g^{-1}). And no obvious change could be noticed in the adsorption capacity on per specific surface area of 0.5 ET (0.034 μmol m^{-2}) compared with PT (0.033 μmol m^{-2}), which indicated that the improved adsorption amount can be ascribed to the increase of the specific surface area (Table 1). Particularly, nanocomposite material showed the highest adsorption capacity (3.91 μmol g^{-1}), which increased by 1.2 and 3.6 times in contrast to 0.5 ET and PT, respectively. However, it was interesting to observe that the adsorption quantity of 0.5rGO/0.5 ET was improved without evident change in the specific surface area (Table 1), as demonstrated by the adsorption capacity on per specific surface area of catalysts increasing from 0.034 μmol m^{-2} (0.5 ET) to 0.073 μmol m^{-2} (0.5rGO/0.5 ET). This showed that rGO provided extra adsorption sites (about 0.039 μmol m^{-2}) for 0.5 ET sample after coupling with rGO. Similarly, TCD signals of 0.5rGO/0.5 ET towards *o*-xylene was higher than that of 0.5 ET and PT, demonstrating that nanocomposite possessed a better adsorption capacity compared with 0.5 ET and PT (Fig. S16). Besides, the chemical desorption peak of 0.5rGO/0.5 ET was higher than that of 0.5 ET and PT, indicating the intermediate species more attached to the nanocomposite surface. This mechanism was further confirmed by NH_3-TPD data, photocatalytic degradation of *o*-xylene over 0.5rGO/PT, and photocurrent response, PL spectra, EIS plots and ESR signals of free radicals during the process of *o*-xylene degradation. Firstly, we carried out NH_3-TPD to analyze the surface changes in the active site. As indicated by the dashed lines in Fig. S19, the additional bands (348 ℃) might be attributed to the desorption of the intermediates. The NH_3-TPD bands of the investigated samples located in 290 ℃ before photocatalytic reaction (the solid lines in Fig. S19). After photodegradation of 4 h, these peak intensities of PT and 0.5 ET significantly decreased, however, the band intensities of 0.5rGO/0.5 ET were not obviously changed (the dashed lines in Fig. S19). This indicated most of the active sites on PT and 0.5 ET surfaces were covered by intermediates while the active sites on 0.5rGO/0.5 ET surface were basically unaffected by intermediates. This phenomenon directly evidenced that rGO can provide extra adsorption sites for intermediate species.

Additionally, as indicated in Fig. S20, interestingly, no significant decline of photocatalytic activity was observed in 0.5rGO/PT compared with PT sample after degradation 240 min, which was also attributed to the combination of rGO providing more adsorption sites (0.046 μmol m^{-2}) for the produced intermediates without obvious change of S_{BET} (Table S4). This further suggested that rGO played a key role in accommodating intermediates. Notably, when the initial concentration of *o*-xylene was increased from 25 ppm to 50 ppm and 100 ppm, respectively, 0.5rGO/0.5 ET keep its activity in the whole reaction time of 240 min. Furthermore, the photocatalyst still kept good durability after four cycles of degradation tests (S21). This again proved that rGO had a good ability to maintain the activity of the photocatalyst 0.5rGO/0.5 ET.

To deeply understand the generated intermediates adsorbed onto the rGO leading to the changes of photogenerated charges and free radicals, we carried out photocurrent and DMPO capture experiments. Fig. 9 shows photocurrent response and PL spectra of 0.5rGO/0.5 ET samples with increasing photocatalytic reaction time from 0 to 60, 120, 180 and 240 min under maintaining gas-phase VOC connection. The intensities of photocurrent density did not change significantly as the photodegradation time increased (Fig. 9a), which showed that the separation process of photogenerated e^--h^+ pairs was not affected by the produced intermediates. This was due to the fact that most of the formed intermediates accumulated on the rGO, which caused uncovered active sites to continue to separate photoinduced charge. This phenomenon was further evidenced by PL and EIS results. As shown in Fig. 9b and Fig. S22, PL intensities and the EIS Nyquist plots' radius of

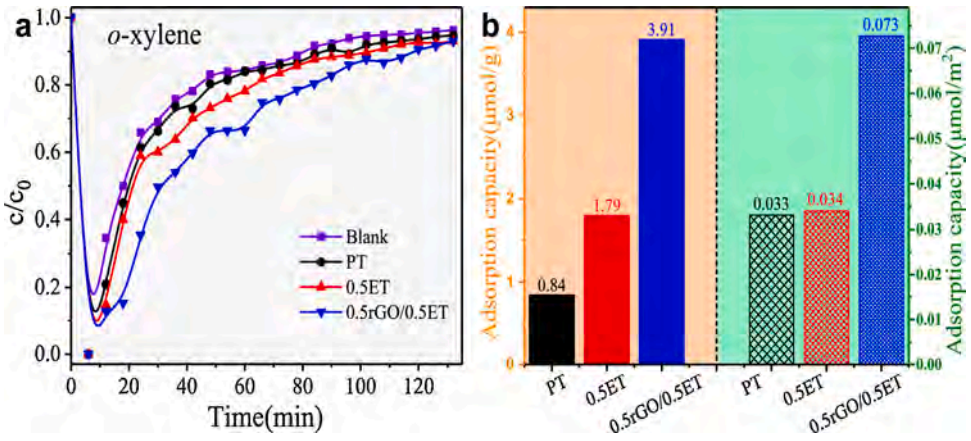

Fig. 8. (a) Dynamic adsorption curves and (b) adsorption capacities (μmol/g) and adsorption capacity on per specific surface area (μmol/m^2) histograms of PT, 0.5 ET and 0.5rGO/0.5 ET samples towards gaseous *o*-xylene under the dark condition.

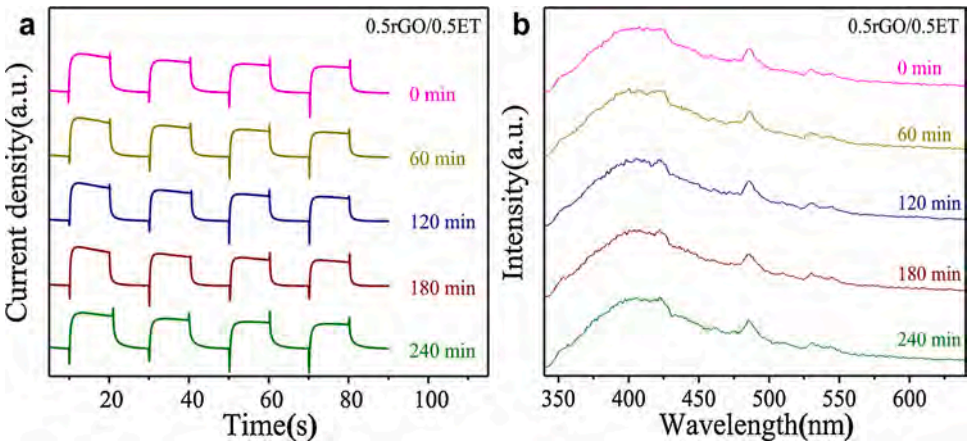

Fig. 9. (a) photocurrent plots and (b) PL spectra of 0.5rGO/0.5 ET catalyst during the process of *o*-xylene degradation.

nanocomposites hardly increased with the increase of lighting time from 0 to 240 min, suggesting that no significant changes occurred in the charge separation process.

The photocatalytic reaction process was closely related to the yield of free radicals ($^{\bullet}OH$ and $^{\bullet}O_2^-$). As presented in Fig. 10a and b, the intensities of $^{\bullet}OH$ and $^{\bullet}O_2^-$ radicals in 0.5rGO/0.5 ET catalyst showed no obvious change as the illumination time increased from 0 to 240 min although some byproducts accumulated on the surface of composites in the process of VOC elimination. This indicated that the reactive sites producing free radicals of the photocatalyst were not covered by intermediates, which due to rGO providing adsorption sites for the generation of intermediates. Therefore, the combination of rGO can make the catalyst maintain high photocatalytic activity (non-deactivation) during the process of gas-phase *o*-xylene elimination although more intermediate species formed on 0.5rGO/0.5 ET surface.

Based on our results, the improved photocatalytic activity of the composite structures, possible reaction pathway of VOC degradation, and deactivation and activation of the investigated photocatalyst are summarized in Scheme 1. Initially, the adsorption-desorption equilibrium is achieved under flowing gaseous *o*-xylene on the catalysts surface (saturated adsorption). Next, free radicals (i.e., $^{\bullet}OH$ and $^{\bullet}O_2^-$) are produced on the catalyst surface under light irradiation which will eventually react with the target pollutants. Notably, the enhanced photocatalytic performance of 0.5rGO/0.5 ET can possibly be due to the following aspects: i) the adsorption ability of the composites was significantly improved in contrast to PT and 0.5 ET (Fig. 8); ii) the incorporation of Er ions induced new RE-4f levels, improving the photogenerated charges separation; iii) the hybridization of rGO promoted electron transfer, as well as the induced RE-4f states reduced electrons transfer barrier between TiO_2 and rGO, further increasing the separation efficiency of carries, and subsequently enhancing the yield of free radicals (Fig. S3). All these features lead to the increased catalytic activity of the composite. Besides, the specific oxidation process was as follows: At first, *o*-xylene is oxidized by free radicals to intermediates with an aromatic ring structure, and then decompose further into the open ring compounds, which would finally react and form water and CO_2. The accumulation of the produced byproducts could cover the reactive sites on the photocatalyst surface, resulting in negative influence its competitive degradation with *o*-xylene. This brought more and more intermediates accumulating on the surface of catalysts, depressing the production of free radical, and eventually leading to the deactivation of the catalyst. It has been observed that the activity of the photocatalysts can be restored when the intermediates are further degraded under continuous light illumination of 2 h, which would otherwise adsorb and cover the actives surfer sites. Interestingly, the introduction of rGO provided more adsorption sites not only for the target VOC, but also for the accumulation of intermediates compared with PT and 0.5 ET (Fig. 8), causing exposing reactive sites to produce free radicals, thereby leading to activation or non-deactivation of photocatalytic activity. Therefore, it is essential to extend the service life of the catalyst for the real application. Also, it is very urgent to find appropriate materials to decorate with TiO_2. Just like rGO, which acted as a trapping agent or a sacrificial agent to capture the intermediates, so that the active sites of the photocatalyst were not covered, and ultimately maintaining the stable and efficient performance of the photocatalyst.

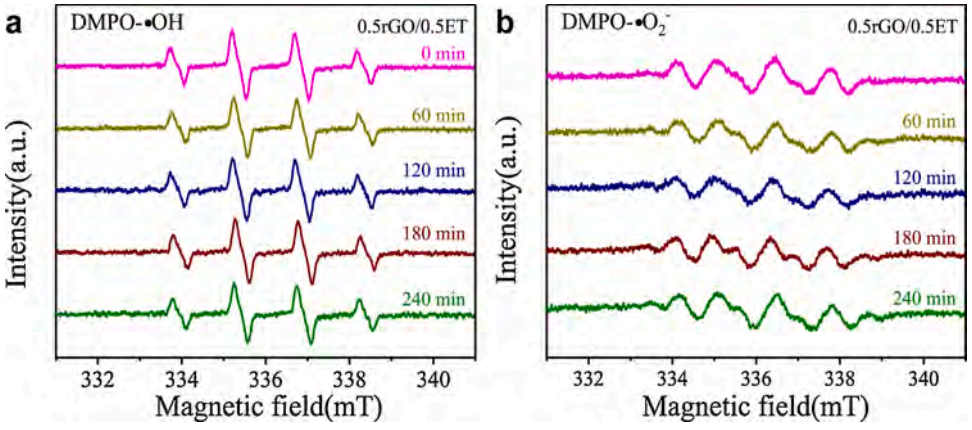

Fig. 10. ESR spectra of (a) DMPO- $^{\bullet}O_2^-$ and (b) DMPO- $^{\bullet}OH$ adducts for 0.5rGO/0.5 ET nanocomposites under different photodegradation time.

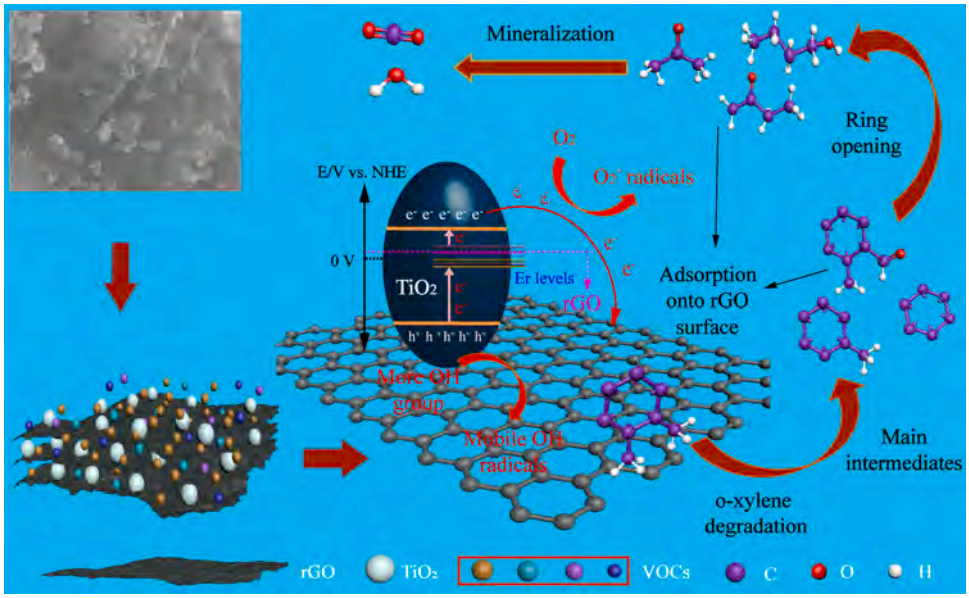

Scheme 1. Schematic diagram of enhancing photocatalytic activity and the proposed reaction routes for VOC photodegradation. rGO provides additional adsorption sites for accommodating intermediates to resist the deactivation of the photocatalyst.

4. Conclusion

In summary, the photocatalytic activity of the PT and 0.5 ET samples towards *o*-xylene diminished with increasing reaction time, i.e., >1 h. The results suggested that the subsequent adsorption of intermediates on the catalyst surface in the course of degradation gradually impeded the production and migration of photoinduced electron-hole pairs, which undoubtedly suppressed the production of free radicals. This ultimately resulted in the catalyst deactivation. To overcome this issue, we have successfully synthesized the 0.5rGO/0.5 ET photocatalyst. The experiments revealed that rGO provide additional adsorption sites on per specific surface area for the generation of intermediate species in contrast to PT and 0.5 ET samples, and hence, more intermediates can be accommodated without fully covering the active reactive sites. This characteristic behavior led to the outstanding and stable photocatalytic performances of the composite even when the reaction time was increased up to 600 min. This work proposed the synthesis of a sustainable and efficient photocatalyst framework for the VOCs abatement, as well as discuss the deactivation and activation mechanism in detail, which can be exploited for the commercial applications.

Supporting information

Experimental setup for photocatalytic oxidation gaseous VOC, XRD and UV–vis spectra of PT, 0.5ET and 0.5rGO/0.5ET photocatalysts. Raman spectra, C 1s and Ti 2p XPS spectra, ESR signals, PL spectra, photocurrent curves, EIS plots, and ESR results of DMPO- $^{\bullet}OH$ and DMPO- $^{\bullet}O_2^-$ adducts of the investigated samples before the photocatalytic reaction. MS results of the generated products in the process of *o*-xylene degradation and *o*-xylene-TPD plots of PT, 0.5 ET and 0.5rGO/0.5 ET catalysts. XRD and ESR data of the investigated samples after the photodegradation of *o*-xylene. Photocurrent, PL, EIS and ESR results of DMPO- $^{\bullet}OH$ and DMPO- $^{\bullet}O_2^-$ adducts for PT and 0.5 ET photocatalysts during the process of photocatalytic reaction. Photocatalytic degradation curves of 0.5rGO/0.5 ET catalyst under irradiation for 600 min, TG curves of PT, 0.5 ET and 0.5rGO/0.5 ET samples before the photodegradation of *o*-xylene under the argon flux. Photodegradation, CO_2 generation and dynamic adsorption plots for gaseous *o*-xylene of 0.5rGO/PT sample. EIS spectra of 0.5rGO/0.5 ET sample during the process of gas-phase *o*-xylene degradation. Main fragment MS signals of the intermediates No. 1- 11 under different retention times. S_{BET} data and adsorption capacity of 0.5rGO/PT sample.

CRediT authorship contribution statement

Zepeng Rao: Conceptualization, Investigation, Methodology, Formal analysis, Data curation, Funding acquisition, Writing - original draft. **Guanhong Lu:** Formal analysis, Investigation, Resources. **Asad Mahmood:** Formal analysis, Funding acquisition. **Gansheng Shi:** Formal analysis. **Xiaofeng Xie:** Investigation, Validation, Funding acquisition, Resources, Project administration. **Jing Sun:** Conceptualization, Methodology, Resources, Funding acquisition, Project administration, Validation, Supervision, Writing - review & editing.

Declaration of Competing Interest

The authors declare that they have no known competing financial interests or personal relationships that could have appeared to influence the work reported in this paper.

Acknowledgment

This work was financially supported by the National Key Research and Development Program of China (2016YFA0203000), Shanghai Commission of Science and Technology Program (19DZ1202600, 20DZ1204100), the National Natural Science Foundation of China (Grant No. 41907303), the Innovation Fund of SICCAS (No. Y91ZC5150G).

Appendix A. Supplementary data

Supplementary material related to this article can be found, in the online version, at doi:https://doi.org/10.1016/j.apcatb.2020.119813.

References

[1] J. Chen, Y. Huang, G. Li, T. An, Y. Hu, Y. Li, VOCs elimination and health risk reduction in e-waste dismantling workshop using integrated techniques of electrostatic precipitation with advanced oxidation technologies, J. Hazard. Mater. 302 (2016) 395–403.

[2] C. He, J. Cheng, X. Zhang, M. Douthwaite, S. Pattisson, Z. Hao, Recent advances in the catalytic oxidation of volatile organic compounds: a review based on pollutant sorts and sources, Chem. Rev. 119 (2019) 4471–4568.

[3] C.L. Bianchi, S. Gatto, C. Pirola, A. Naldoni, A. Di Michele, G. Cerrato, V. Crocellà, V. Capucci, Photocatalytic degradation of acetone, acetaldehyde and toluene in gas-phase: comparison between nano and micro-sized TiO_2, Appl. Catal. B 146 (2014) 123–130.

[4] J.D. Spengler, K. Sexton, Indoor air pollution: a public health perspective, Science 221 (1983) 9–17.

[5] U. Pöschl, M. Shiraiwa, Multiphase chemistry at the atmosphere–biosphere interface influencing climate and public health in the anthropocene, Chem. Rev. 115 (2015) 4440–4475.

[6] R.J. Huang, Y. Zhang, C. Bozzetti, K.F. Ho, J.J. Cao, Y. Han, K.R. Daellenbach, J. G. Slowik, S.M. Platt, F. Canonaco, P. Zotter, R. Wolf, S.M. Pieber, E.A. Bruns, M. Crippa, G. Ciarelli, A. Piazzalunga, M. Schwikowski, G. Abbaszade, J. Schnelle-Kreis, R. Zimmermann, Z. An, S. Szidat, U. Baltensperger, I.E. Haddad, A.S. Prevot, High secondary aerosol contribution to particulate pollution during haze events in China, Nature 514 (2014) 218–222.

[7] A.H. Mamaghani, F. Haghighat, C.S. Lee, Photocatalytic oxidation technology for indoor environment air purification: the state-of-the-art, Appl. Catal. B 203 (2017) 247–269.

[8] Y. Boyjoo, H. Sun, J. Liu, V.K. Pareek, S. Wang, A review on photocatalysis for air treatment: from catalyst development to reactor design, Chem. Eng. J. 310 (2017) 537–559.

[9] H. Chen, C.E. Nanayakkara, V.H. Grassian, Titanium dioxide photocatalysis in atmospheric chemistry, Chem. Rev. 112 (2012) 5919–5948.

[10] Z. Shayegan, C.S. Lee, F. Haghighat, TiO_2 photocatalyst for removal of volatile organic compounds in gas phase – a review, Chem. Eng. J. 334 (2018) 2408–2439.

[11] Y. Guo, M. Wen, G. Li, T. An, Recent advances in VOC elimination by catalytic oxidation technology onto various nanoparticles catalysts: a critical review, Appl. Catal. B 281 (2021), 119447.

[12] I. Dhada, M. Sharma, P.K. Nagar, Quantification and human health risk assessment of by-products of photo catalytic oxidation of ethylbenzene, xylene and toluene in indoor air of analytical laboratories, J. Hazard. Mater. 316 (2016) 1–10.

[13] W. Zhang, G. Li, H. Liu, J. Chen, S. Ma, M. Wen, J. Kong, T. An, Photocatalytic degradation mechanism of gaseous styrene over Au/TiO_2@CNTs: relevance of superficial state with deactivation mechanism, Appl. Catal. B 272 (2020), 118969.

[14] P. Chen, W. Cui, H. Wang, X. Dong, J. Li, Y. Sun, Y. Zhou, Y. Zhang, F. Dong, The importance of intermediates ring-opening in preventing photocatalyst deactivation during toluene decomposition, Appl. Catal. B 272 (2020), 118977.

[15] S. Weon, F. He, W. Choi, Status and challenges in photocatalytic nanotechnology for cleaning air polluted with volatile organic compounds: visible light utilization and catalyst deactivation, Environ. Sci-Nano 6 (2019) 3185–3214.

[16] X. Dong, W. Cui, H. Wang, J. Li, Y. Sun, H. Wang, Y. Zhang, H. Huang, F. Dong, Promoting ring-opening efficiency for suppressing toxic intermediates during photocatalytic toluene degradation via surface oxygen vacancies, Sci. Bull. 64 (2019) 669–678.

[17] Z. Lu, M. Piernavieja-Hermida, C.H. Turner, Z. Wu, Y. Lei, Effects of TiO_2 in low temperature propylene epoxidation using gold catalysts, J. Phys. Chem. C 122 (2018) 1688–1698.

[18] S. Weon, W. Choi, TiO_2 nanotubes with open channels as deactivation-resistant photocatalyst for the degradation of volatile organic compounds, Environ. Sci. Technol. 50 (2016) 2556–2563.

[19] J. Chen, Z. He, Y. Ji, G. Li, T. An, W. Choi, OH radicals determined photocatalytic degradation mechanisms of gaseous styrene in TiO_2 system under 254 nm versus 185 nm irradiation: combined experimental and theoretical studies, Appl. Catal. B 257 (2019), 117912.

[20] M. Hosseini, S. Siffert, H.L. Tidahy, R. Cousin, J.F. Lamonier, A. Aboukais, A. Vantomme, M. Roussel, B.L. Su, Promotional effect of gold added to palladium supported on a new mesoporous TiO_2 for total oxidation of volatile organic compounds, Catal. Today 122 (2007) 391–396.

[21] P. Mazierski, A. Mikolajczyk, B. Bajorowicz, A. Malankowska, A. Zaleska-Medynska, J. Nadolna, The role of lanthanides in TiO_2-based photocatalysis: a review, Appl. Catal. B 233 (2018) 301–317.

[22] J. Zhou, Q. Liu, W. Feng, Y. Sun, F. Li, Upconversion luminescent materials: advances and applications, Chem. Rev. 115 (2015) 395–465.

[23] Z. Rao, X. Xie, X. Wang, A. Mahmood, S. Tong, M. Ge, J. Sun, Defect chemistry of Er^{3+}-doped TiO_2 and its photocatalytic activity for the degradation of flowing gas-phase VOCs, J. Phys. Chem. C 123 (2019) 12321–12334.

[24] Z. Rao, G. Shi, Z. Wang, A. Mahmood, X. Xie, J. Sun, Photocatalytic degradation of gaseous VOCs over Tm^{3+}-TiO_2: revealing the activity enhancement mechanism and different reaction paths, Chem. Eng. J. 395 (2020), 125078.

[25] R. Ma, Y. Zhou, H. Bi, M. Yang, J. Wang, Q. Liu, F. Huang, Multidimensional graphene structures and beyond: unique properties, syntheses and applications, Prog. Mater. Sci. 113 (2020), 100665.

[26] C.K. Chua, M. Pumera, Chemical reduction of graphene oxide: a synthetic chemistry viewpoint, Chem. Soc. Rev. 43 (2014) 291–312.

[27] F.K. Laura, J. Cote, J. Huang, Langmuir-blodgett assembly of graphite oxide single layers, J. Am. Chem. Soc. 131 (2009) 1043–1049.

[28] W.A. Saoud, A.A. Assadi, M. Guiza, A. Bouzaza, W. Aboussaoud, I. Soutrel, A. Ouederni, D. Wolbert, S. Rtimi, Abatement of ammonia and butyraldehyde under non-thermal plasma and photocatalysis: oxidation processes for the removal of mixture pollutants at pilot scale, Chem. Eng. J. 344 (2018) 165–172.

[29] W. Lin, X. Xie, X. Wang, Y. Wang, D. Segets, J. Sun, Efficient adsorption and sustainable degradation of gaseous acetaldehyde and o-xylene using rGO-TiO_2 photocatalyst, Chem. Eng. J. 349 (2018) 708–718.

[30] F. Wang, Y. Han, C.S. Lim, Y. Lu, J. Wang, J. Xu, H. Chen, C. Zhang, M. Hong, X. Liu, Simultaneous phase and size control of upconversion nanocrystals through lanthanide doping, Nature 463 (2010) 1061–1065.

[31] S. Obregón, A. Kubacka, M. Fernández-García, G. Colón, High-performance Er^{3+}–TiO_2 system: dual up-conversion and electronic role of the lanthanide, J. Catal. 299 (2013) 298–306.

[32] K.N. Kudin, B. Ozbaas, H.C. Schniepp, R.K. Prud'homme, Raman spectra of graphite oxide and functionalized graphene sheets, Nano Lett. 8 (2008) 36–41.

[33] Y. Matsumoto, M. Koinuma, S.Y. Kim, Y. Watanabe, T. Taniguchi, K. Hatakeyama, H. Tateishi, S. Ida, Simple photoreduction of graphene oxide nanosheet under mild conditions, ACS Appl. Mater. Inter. 2 (2010) 3461–3466.

[34] G. Rajender, J. Kumar, P.K. Giri, Interfacial charge transfer in oxygen deficient TiO_2-graphene quantum dot hybrid and its influence on the enhanced visible light photocatalysis, Appl. Catal. B 224 (2018) 960–972.

[35] J. Reszczyńska, T. Grzyb, J.W. Sobczak, W. Lisowski, M. Gazda, B. Ohtani, A. Zaleska, Visible light activity of rare earth metal doped (Er^{3+}, Yb^{3+} or Er^{3+}/Yb^{3+}) titania photocatalysts, Appl. Catal. B 163 (2015) 40–49.

[36] D. Li, H. Haneda, S. Hishita, N. Ohashi, Visible-light-driven N-F-codoped TiO_2 photocatalysts. 2. Optical characterization, photocatalysis, and potential application to air purification, Chem. Mater. 17 (2005) 2596–2602.

[37] J.S. Lee, K.H. You, C.B. Park, Highly photoactive, low bandgap TiO_2 nanoparticles wrapped by graphene, Adv. Mater. 24 (2012) 1084–1088.

[38] R. Wang, C. Xu, J. Sun, L. Gao, C. Lin, Flexible free-standing hollow Fe_3O_4/graphene hybrid films for lithium-ion batteries, J. Mater. Chem. A 1 (2013) 1794–1800.

[39] J. Li, X. Dong, G. Zhang, W. Cui, W. Cen, Z. Wu, S.C. Lee, F. Dong, Probing ring-opening pathways for efficient photocatalytic toluene decomposition, J. Mater. Chem. A 7 (2019) 3366–3374.

[40] F. Zhang, X. Li, Q. Zhao, Q. Zhang, M. Tade, S. Liu, Fabrication of alpha-Fe_2O_3/In_2O_3 composite hollow microspheres: a novel hybrid photocatalyst for toluene degradation under visible light, J. Colloid. Interf. Sci. 457 (2015) 18–26.

[41] O. Marie, F. Thibaultstarzyk, P. Massiani, Conversion of xylene over mordenites: an operando infrared spectroscopy study of the effect of Na+, J. Catal. 230 (2005) 28–37.

[42] A.H. Mamaghani, F. Haghighat, C.-S. Lee, Gas phase adsorption of volatile organic compounds onto titanium dioxide photocatalysts, Chem. Eng. J. 337 (2018) 60–73.

[43] E.L. Hommel, H.C. Allen, The air–liquid interface of benzene, toluene, m-xylene, and mesitylene: a sum frequency, Raman, and infrared spectroscopic study, Analyst. 128 (2003) 750–755.

[44] J. Liu, Y. Li, J. Ke, S. Wang, L. Wang, H. Xiao, Black NiO-TiO_2 nanorods for solar photocatalysis: recognition of electronic structure and reaction mechanism, Appl. Catal. B 224 (2018) 705–714.

[45] M. Lai, J. Zhao, Q. Chen, S. Feng, Y. Bai, Y. Li, C. Wang, Photocatalytic toluene degradation over Bi-decorated TiO_2: promoted O_2 supply to catalyst's surface by metallic Bi, Catal. Today 335 (2019) 372–380.

[46] X. Li, Z. Zhu, Q. Zhao, S. Liu, FT-IR study of the photocatalytic degradation of gaseous toluene over UV-irradiated TiO_2 microballs: enhanced performance by hydrothermal treatment in alkaline solution, Appl. Surf. Sci. 257 (2011) 4709–4714.

[47] H. Niu, K. Li, B. Chu, W. Su, J. Li, Heterogeneous reactions between toluene and NO_2 on mineral particles under simulated atmospheric conditions, Environ. Sci. Technol. 51 (2017) 9596–9604.

[48] M.D. Hernández-Alonso, I. Tejedor-Tejedor, J.M. Coronado, M.A. Anderson, Operando FTIR study of the photocatalytic oxidation of methylcyclohexane and toluene in air over TiO_2–ZrO_2 thin films: influence of the aromaticity of the target molecule on deactivation, Appl. Catal. B 101 (2011) 283–293.

[49] M. Jang, S.R. Mcdow, Products of benz[a]anthracene photodegradation in the presence of known organic constituents of atmospheric aerosols, Environ. Sci. Technol. 31 (1997) 1046–1053.

[50] M.M. Ameen, G.B. Raupp, Reversible catalyst deactivation in the photocatalytic oxidation of dilute o-xylene in air, J. Catal. 184 (1999) 112–122.

[51] Y. Nosaka, A.Y. Nosaka, Generation and detection of reactive oxygen species in photocatalysis, Chem. Rev. 117 (2017) 11302–11336.

[52] H. Wang, S. Jiang, S. Chen, D. Li, X. Zhang, W. Shao, X. Sun, J. Xie, Z. Zhao, Q. Zhang, Y. Tian, Y. Xie, Enhanced singlet oxygen generation in oxidized graphitic carbon nitride for organic synthesis, Adv. Mater. 28 (2016) 6940–6945.